DIRECT INVERSION OF YOUNG'S MODULUS AND POISSON'S RATIO USING EXACT ZOEPPRITZ EQUATIONS BASED ON DOUBLE CONSTRAINTS

QIQI MA and ZANDONG SUN

China University of Petroleum (Beijing), Beijing 102249, P.R. China.
ma_qi_qi@163.com; szd@cup.edu.cn

ABSTRACT

Ma, Q.Q. and Sun, Z.D., 2019. Direct inversion of Young's modulus and Poisson's ratio using exact Zoeppritz equations based on double constraints. *Journal of Seismic Exploration*, 28: 175-204.

Young's modulus and Poisson's ratio are important elastic parameters that can be derived from prestack seismic inversion and subsequently used to evaluate rock brittleness, fluid discrimination, and predict sweet-spots for oil and gas production. Conventionally, Young's modulus and Poisson's ratio are estimated indirectly from P-wave, S-wave, and density data according to well-established petrophysical relationships or computed directly from the approximate equations. However, the former approach can introduce uncertainties in the calculation of Young's modulus and Poisson's ratio because of accumulated biases and the difficulty of calculating density. The latter approach can also generate uncertainties, because the inversion method based on the approximate equations has poor performance with regards to utilizing far offset seismic amplitude information. Therefore, the novel exact Zoeppritz equations are applied to obtain more stable and accurate values of Young's modulus and Poisson's ratio. Firstly, a set of new forms of exact equations in terms of Young's modulus reflectivity, Poisson's ratio reflectivity, and density reflectivity are derived. Then, Bayesian theory and double constraints are introduced to construct the objective function. The double constraints include the Trivariate Cauchy distribution constraint and the modified low-frequency constraint. The Trivariate Cauchy constraint can improve vertical resolution of inversion results. The modified low-frequency constraint can obtain more reliable low-frequency information without reducing the resolution of inversion results. The objective function is complicated. The ideas of generalized linear inversion and the iterative reweighed least-squares algorithm are applied to solve this function. Tests with synthetic data show that the inverted Young's modulus and Poisson's ratio of the proposed method are still reasonable in moderate noise condition. Tests with field data show that the inverted results agree well with well-logging data.

KEY WORDS: Young's modulus, Poisson's ratio, generalized linear inversion,
                        exact Zoeppritz equations, Bayesian inversion, double constraints.

INTRODUCTION

With the increasing demand for energy, the emphasis of oil and gas exploration has shifted from conventional to unconventional oil and gas resources (Sun et al., 2011). Methods of identifying potential hydrocarbon accumulations from seismic data, known as quantitative interpretation, have been popular since the 1970s and 80s, starting with bright-spot and amplitude-versus-offset analysis (Castagna and Backus, 1993; Ostrander, 1984; Shuey, 1985). More recently, obtaining elastic parameters that can reflect the lithology and fluid properties from stacked and pre-stack seismic data has been a popular research area in exploration geophysics (Avseth et al., 2005; Gidlow et al., 2003; Quakenbush et al., 2006). Brittleness index plays an important role in unconventional oil and gas exploration (Yang et al., 2015).

Estimating specific petrophysical parameters directly from pre-stack data may result in greater physical insight than traditional parameters, like P-wave velocity, S-wave velocity, and density. For example, reservoir geophysicists proposed using brittle mineral content in rocks (Mavko, 2010; Yang et al., 2015) and elastic parameters (Altindag, 2002; Guo et al., 2012; Liu et al., 2015; Rickman et al., 2008) to construct brittleness evaluation parameters. According to Liu et al. (2015), Ritesh et al. (2013), and Sena et al. (2011) for example, Young's modulus and Poisson's ratio could be used to evaluate brittleness index and hydrocarbon fluid discrimination, and predict "sweet-spots" for oil and gas production. Ostrander (1984) showed that high-porosity gas-bearing sandstones had anomalously low values of Poisson's ratio. Conventionally, Young's modulus and Poisson's ratio are calculated indirectly from P-wave, S-wave, and density data, which can be calculated directly by pre-stack inversion (Sena et al., 2011). However, it is difficult to estimate the density data and results are often unstable (Downton, 2005; Khare et al., 2007; Liu et al., 2012; Shi et al., 2010). Moreover, the indirect calculation methods mentioned above can lead to cumulative bias (Zong et al., 2012). Zong et al. (2012, 2013) derived a new approximate equation based on Young's modulus and Poisson's ratio, and established an elastic impedance inversion method for Young's modulus and Poisson's ratio. However, all these studies were based on the approximate Zoeppritz equations. These approximate equations satisfy the requirements of small-to-moderate incident angles and weak reflection coefficients (Aki and Richards, 1980; Jun et al., 2015). Therefore, using the approximate equations to estimate Young's modulus and Poisson's ratio usually limits the accuracy of inversion results in scenarios that do not meet these assumptions. In contrast, utilizing the exact Zoeppritz equations can not only avoid the cumulative bias introduced by approximate equations but can also directly and conveniently invert the elastic parameters, which improves the accuracy and robustness of inversion (Behura et al., 2010; Huang et al., 2015; Tarantola et al., 1986; Zhou et al., 2017).

In this study, we propose a direct inversion method of Young's modulus and Poisson's ratio, based on an exact formulation of the Zoeppritz equations. It has the advantage of not using density data, thereby avoiding

the accumulated errors of indirect methods, and being accurate in situations of large incident angles or strong reflection coefficients. The next section will explain the derivation of this novel method.

The forward operators of the exact Zoeppritz equations are complex and nonlinear. Intelligent algorithms and GLI are usually used to solve nonlinear problems (Zhou et al., 2017). Although many researchers have studied intelligent algorithms (Bai et al., 2014; Priezzhev et al., 2008; Veeken et al., 2009; Yang et al., 2008; Yuan et al., 2009; Zhang et al., 2007), they have not been widely adopted because of their huge computational complexity. Generalized linear inversion (GLI) is based on Taylor's series expansions (Cooke et al., 1983). Theoretically, after several iterations, highly accurate inversion results can be achieved. Researchers such as Kurt (2007), Larsen et al. (1999), Li et al. (2010), Lu et al. (2015), Zhang et al. (2013), and Zhou et al. (2016) have reported on improvements to the stability of the method when inverting seismic data to obtain P-wave, S-wave, and density parameters. However, the Jacobian matrix, which is the core of the GLI calculation, is often a source of instability in the inversion due to an excessively large conditional number. Therefore, it is necessary to add appropriate regularization constraints to the objective function for improving the stability of the inversion.

In Bayesian inversion, the posterior probability distributions of the model parameters are generated by introducing the prior information of the model parameters and the likelihood function of the noise. The minimum value of the inversion objective function can be converted into the maximization problem of the posterior probability distribution. Introducing the prior information of model parameters as a regularization constraint of inversion can effectively improve the ill-posed nature of the inversion problem. The prior information of the model parameters can follow different statistical distributions, depending upon the situation. Buland and Omre (2003) created a linearized AVO inversion method based on the Bayesian framework. Karimi et al. (2010) proposed a Bayesian closed-skew Gaussian inversion method in which the posterior probability distribution obeyed a skew probability density function. Downton et al. (2005) proposed that the reflection coefficients obeyed three different types of long-tail distributions, which improved the resolution of the inversion relative to the results of Gaussian distributions. Considering the geological background, Alemie and Sacchi (2011) introduced a Trivariate Cauchy prior distribution for regularizing the ill-posed problem of AVO inversion. Compared with univariate statistical distributions, this method considered the statistical correlation among the three parameters, which increased the reliability and accuracy of inversion results.

Relative acoustic impedance can be transformed into the absolute impedance by merging reliable low-frequency model information (Cerney and Bartel, 2007). This low-frequency information not only provides an overall level to the data, it also increases the bandwidth and hence increases the resolution and accuracy (Berkhout, 1997) of the inversion results. The low-frequency information of seismic data is related to the seismic source and

acquisition techniques. Presently, the lowest frequency of the low-frequency vibrator is about 3 Hz (Tao et al., 2011), and the lowest frequency of the geophone is about 2 Hz (Li et al., 2013). However, because of the huge cost of low-frequency seismic data acquisition, conventional seismic acquisition methods use 5 Hz for the source and 10 Hz for the receiver (Zhang et al., 2015). That is, seismic data with frequency lower than 10 Hz is seriously affected by noise. Moreover, surface wave suppression also affects the low-frequency component. The prior distributions mentioned above are only related to the vertical resolution of the inversion results; the low-frequency component, cannot be obtained directly from the seismic data, thus other constraints are required. Many studies have used a smoothing constraint to improve the noise-reducing performance of the inversion and supplement the low-frequency information of the inversion results (Tian et al., 2013; Zong et al., 2012). Although the smoothing constraint term can supplement the low-frequency component of the inversion results, selecting suitable weights for the constraint terms can be difficult. Inappropriate weights may result in a reduction of the resolution of the inversion results. Zhang et al. (2016) introduced a soft low-frequency constraint, which can improve the robustness and the adaptability of the inversion results.

Building on the previous studies, we propose and implement an innovative technique for the direct extraction of the Young's modulus and Poisson's ratio from pre-stack seismic data. To improve the accuracy of inverting data with large angles of incidence, the method utilizes GLI based on exact Zoeppritz equations to construct forward operators in terms of Young's modulus and Poisson's ratio. Meanwhile, combining the Bayesian theory, the Gaussian distribution is used for the likelihood function and the Trivariate Cauchy distribution is used for the prior distribution of the model parameters. In this way, the ill-posedness of the problem can be effectively reduced. Then, we introduce a low-pass filter matrix to construct a low-frequency constraint term. The modified low-frequency constraint term can not only obtain stable low-frequency information but also does not reduce the resolution or accuracy of the inversion results. Because the objective function is nonlinear. The iterative reweighted least-squares algorithm is applied for solving the optimization problem.

THEORY

Exact Zoeppritz equations expressed in terms of Young's modulus and Poisson's ratio

To avoid the calculation error introduced by approximate equations, we use the exact Zoeppritz equations to construct the AVO forward operators. Knott (1899) and Zoeppritz (1919) derived the exact equations of the reflection and transmission coefficients. These equations are functions of the incident angles and elastic parameters of the medium. The exact Zoeppritz equations assume that two solid half-spaces are welded at an elastic interface. In this paper, we denote the P-wave velocity, S-wave velocity, and density of the upper half-space by V_{p1}, V_{s1} and ρ_1, respectively; V_{p2}, V_{s2} and ρ_2 denote

the same for the lower half-space, respectively. Using the exact Zoeppritz equations, reflection and transmission coefficients of P-wave and S-wave (R_{pp}, R_{PS}, T_{PP}, T_{PS}) can be described.

$$
\begin{bmatrix}
\sin a & \cos b & -\sin a' & \cos b' \\
\cos a & -\sin b & \cos a' & \sin b' \\
\sin 2a & \dfrac{V_{p1}}{V_{s1}}\cos 2b & \dfrac{V_{p1}}{V_{p2}}\dfrac{V_{s2}^2}{V_{s1}^2}\dfrac{\rho_2}{\rho_1}\sin 2a' & -\dfrac{\rho_2}{\rho_1}\dfrac{V_{p1}V_{s2}}{V_{s1}^2}\cos 2b' \\
\cos 2b & -\dfrac{V_{s1}}{V_{p1}}\sin 2b & -\dfrac{\rho_2}{\rho_1}\dfrac{V_{p2}}{V_{p1}}\cos 2b' & -\dfrac{\rho_2}{\rho_1}\dfrac{V_{s2}}{V_{p1}}\sin 2b'
\end{bmatrix}
\begin{bmatrix}
R_{pp} \\ R_{PS} \\ T_{PP} \\ T_{PS}
\end{bmatrix}
=
\begin{bmatrix}
-\sin a \\ \cos a \\ \sin 2a \\ -\cos 2b
\end{bmatrix}
\qquad (1)
$$

where a and b represent the P-wave incident angle and the S-wave reflected angle at the interface, respectively, and a' and b' denote the P-wave transmitted angle and S-wave transmitted angle, respectively.

The classical exact Zoeppritz equations are shown in eq. (1). With some parameter substitutions, the classical exact equations can be expressed as new forms of exact equations in terms of Young's modulus reflectivity, Poisson's ratio reflectivity, and density reflectivity. First, the coefficient matrix of eq. (1) can be modified and expressed as a function of P-wave velocity reflectivity, S-wave velocity reflectivity, density reflectivity, and V_{p1}/V_{s1}.

$$
\begin{bmatrix}
\sin a & \cos b & -\sin a' & \cos b' \\
\cos a & -\sin b & \cos a' & \sin b' \\
\sin 2a & \gamma\cos 2b & \dfrac{(2+R_{vs})^2(2+R_d)(2-R_{vp})\sin 2a'}{(2-R_{vs})^2(2-R_d)(2+R_{vp})} & -\dfrac{(2+R_{vs})(2+R_d)\gamma\cos 2b'}{(2-R_{vs})(2-R_d)} \\
\cos 2b & -\dfrac{\sin 2b}{\gamma} & -\dfrac{(2+R_{vp})(2+R_d)\cos 2b'}{(2-R_{vp})(2-R_d)} & -\dfrac{(2+R_{vs})(2+R_d)\sin 2b'}{(2-R_{vs})(2-R_d)\gamma}
\end{bmatrix}
\begin{bmatrix}
R_{pp} \\ R_{ps} \\ T_{pp} \\ T_{ps}
\end{bmatrix}
=
\begin{bmatrix}
-\sin a \\ \cos a \\ \sin 2a \\ -\cos 2b
\end{bmatrix}
$$

$$(2)$$

where

R_{vp} is the P-wave velocity reflectivity

$$
R_{vp} = \frac{\Delta V_p}{V_p} = \frac{2\left(V_{p2}-V_{p1}\right)}{V_{p2}+V_{p1}}
$$

R_{vs} is the S-wave velocity reflectivity

$$R_{vs} = \frac{\Delta V_s}{\overline{V_s}} = \frac{2(V_{s2} - V_{s1})}{V_{s2} + V_{s1}}$$

R_d is the density reflectivity

$$R_d = \frac{\Delta \rho}{\overline{\rho}} = \frac{2(\rho_2 - \rho_1)}{\rho_2 + \rho_1} \; ,$$

and γ is V_{p1} / V_{s1}.

To obtain different elastic parameters more directly and conveniently, many studies have proposed different approximate equation of the exact Zoeppritz equations. Zong et al. (2013) established the relationships among the P-wave modulus reflectivity R_M, S-wave modulus reflectivity R_μ, density reflectivity, Young's modulus reflectivity R_E, and Poisson's ratio reflectivity R_σ, which can be written as

$$R_M = \frac{\Delta M}{\overline{M}} = R_E + \frac{(k-2)^2(3k-2)}{k(3k-4)} R_\sigma \tag{3}$$

$$R_\mu = \frac{\Delta \mu}{\overline{\mu}} = R_E + \frac{2-k}{3k-4} R_\sigma \tag{4}$$

$$R_E = \frac{\Delta E}{\overline{E}} = \frac{2(E_2 - E_1)}{E_2 + E_1} \tag{5}$$

$$R_\sigma = \frac{\Delta \sigma}{\overline{\sigma}} = \frac{2(\sigma_2 - \sigma_1)}{\sigma_2 + \sigma_1} \tag{6}$$

$$k = \frac{\overline{V_s}^2}{\overline{V_p}^2} \; , \tag{7}$$

where Young's modulus and Poisson's ratio of the upper half-space are denoted by E_1 and σ_1, respectively, and E_2 and σ_2 denote the Young's modulus and Poisson's ratio of the lower half-space, respectively; $\overline{V_s}$ is the average S-wave velocity of the upper and lower media, and $\overline{V_p}$ is the average P-wave velocity of the upper and lower media.

By differential transformation, the relationships among P-wave modulus, S-wave modulus, P-wave velocity, S-wave velocity, and density reflectivity can be shown as

$$\frac{\Delta V_p}{V_p} = \frac{1}{2}\left(\frac{\Delta M}{M} - \frac{\Delta \rho}{\rho}\right) \tag{8}$$

$$\frac{\Delta V_s}{V_s} = \frac{1}{2}\left(\frac{\Delta \mu}{\mu} - \frac{\Delta \rho}{\rho}\right) \tag{9}$$

Substituting eqs. $(3) - (9)$ into eq. (2), a new form of the Zoeppritz equations in terms of Young's modulus reflectivity, Poisson's ratio reflectivity, and density reflectivity can be expressed as

$$\begin{bmatrix} \sin a & \cos b & -\sin a' & \cos b' \\ \cos a & -\sin b & \cos a' & \sin b' \\ \sin 2a & \gamma \cos 2b & \dfrac{(2+A)^2(2+C)(2-B)\sin 2a'}{(2-A)^2(2-C)(2+B)} & -\dfrac{(2+A)(2+C)\gamma \cos 2b'}{(2-A)(2-C)} \\ \cos 2b & -\dfrac{\sin 2b}{\gamma} & -\dfrac{(2+B)(2+C)\cos 2b'}{(2-B)(2-C)} & -\dfrac{(2+A)(2+C)\sin 2b'}{(2-A)(2-C)\gamma} \end{bmatrix} \begin{bmatrix} R_{pp} \\ R_{ps} \\ T_{pp} \\ T_{ps} \end{bmatrix} = \begin{bmatrix} -\sin a \\ \cos a \\ \sin 2a \\ -\cos 2b \end{bmatrix} \tag{10}$$

where

$$A = \frac{1}{2}\left(R_E + \frac{(k-2)^2(3k-2)}{k(3k-4)}R_\sigma - R_d\right)$$

$$B = \frac{1}{2}\left(R_E + \frac{2-k}{3k-4}R_\sigma - R_d\right)$$

and $C = R_d$.

Table 1. Fundamental parameters for four classes of AVO anomalies used in synthetic modelling to test our new formulation of the exact Zoeppritz equations.

AVO type	Lithology	V_p m/s	V_s m/s	Density kg/m^3
Class I	Shale	3095	1515	2400
	Gas-bearing sand	4050	2524	2210
Class II	Shale	2645	1170	2290
	Gas-bearing sand	2780	1665	2080
Class III	Shale	2190	820	2160
	Gas-bearing sand	1600	900	1980
Class IV	Shale	3240	1620	2340
	Gas-bearing sand	1650	1090	2070

To compare the accuracy of the new equation with that of the approximate equation of Zong et al. (2013) based on Young's modulus and Poisson's ratio, we conduct a quantitative analysis of four classes of AVO anomalies (Castagna et al., 1997) for a gas-sand overlain by shale. The fundamental parameters of four classes of AVO anomalies are listed in Table 1. Class I is a gas-bearing sand with a higher impedance than the overlying shale. For Class II, the gas-bearing sand has similar impedance to that of the overlying unit. A Class III gas-bearing sand has lower impedance than the overlying shale. As the incident angles become larger, the absolute values of the reflection coefficients become larger. Class IV is similar to Class III: although, for Class IV, as the incident angles become larger, the absolute values of the reflection coefficients become smaller over small-to-moderate angles. We compare the reflection coefficients estimated from the new exact equations (named "new-method" in Fig. 1), the approximate equations of Zong's (2013) (named "YPD" in Fig. 1), and the classical exact equations (named "Zoeppritz" in Fig. 1). The specific formula of "YPD" is

$$R_{pp}(\theta) = \left(\frac{1}{4}\sec^2\theta - 2k\sin^2\theta \right) R_E + \left(\frac{1}{4}\sec^2\theta \frac{(2k-3)(2k-1)^2}{k(4k-3)} + 2k\sin^2\theta \frac{1-2k}{3-4k} \right) R_\sigma + \left(\frac{1}{2} - \frac{1}{4}\sec^2\theta \right) R_d$$

More specifically, Figs. 1a, b, c, and d show the reflection coefficients estimated from the three methods in different kinds of AVO models (Class I, Class II, Class III, and Class IV), respectively. It can be seen from Fig. 1 that the reflection coefficients of the new exact equations are almost identical to those of the classical exact equations; however, the reflection coefficients of the approximate equations are somewhat different. These differences are particularly noticeable in the situation of large incident angles, which is to be expected as the validity of most approximations is typically limited to angles of 30 or 40°.

For eq. (10), γ can be obtained from initial models. R_{pp}, the P-wave reflection coefficient, can be estimated by a nonlinear function [eq. (10)] in terms of R_E, R_σ, and R_d. In our study, these three reflection coefficients are taken as the model parameters to be inverted. Considering the computational complexity, speed of convergence, and the accuracy of convergence, we adopt a GLI to solve the problem. We obtain the forward function:

$$\mathbf{D'} = \mathbf{GM} \quad , \tag{11}$$

where **D'** can be obtained from the observed seismic data and the initial

models, **G** is the forward operator, and **M** is the model parameter; the specific expressions are given in Appendix A**.** In this study, the initial models are generated by extracting the low-frequency data from well-log data. The model parameters can be inverted directly by eq. (11). However, **G** of   eq. (11) has a large condition number, which produces the ill-posed problem. Therefore, it is necessary to introduce the prior distribution of the model parameters' reflection coefficients, according to Bayes' theorem, as a regularization term to make the inversion problem well-conditioned.

(a)   (b)

(c)   (d)
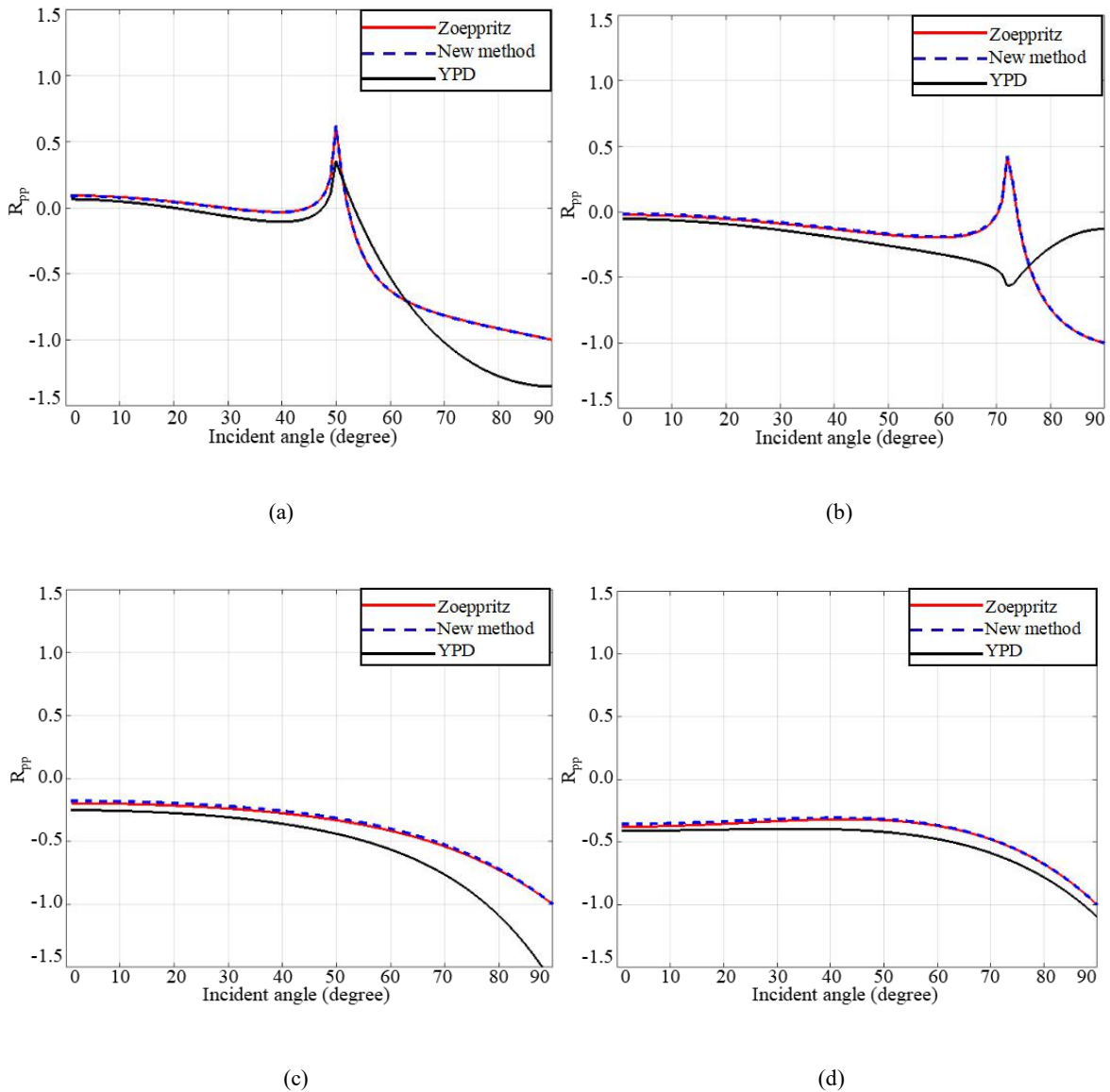
Fig. 1. Comparison of reflection coefficients of the classical exact equations, the approximate equations, and the new exact equations for four classes of AVO anomalies with incident angles from 1 to 90 degrees. (a) AVO Class I; (b) AVO Class II; (c) AVO Class III; (d) AVO Class IV; in all cases the red lines indicate the classical exact equations, the black lines indicate the approximate equations (YPD), and the blue dotted lines indicate the new exact equations.

Objective function

Bayes' theorem can improve the inverted accuracy of elastic parameters by introducing prior information, which can effectively reduce the variance in the statistical distribution of the parameters. Assuming that the elastic parameters of the subsurface medium are in accord with the prior distribution, $P(\mathbf{M})$, where $\mathbf{M}$ represents the model parameter. The noise information for the pre-stack seismic gathers can be obtained by comparison of observed and synthetic seismic data. The noise likelihood function can be written as $P(\mathbf{D'}|\mathbf{M})$. Since the distribution of observed seismic data is only determined by the distribution of the noise, $P(\mathbf{D'}|\mathbf{M})$ also expresses the posterior probability density function of observed seismic data, $\mathbf{D'}$. So, the posterior probability density function of the model parameter $P(\mathbf{M}|\mathbf{D'})$ can be expressed as

$$P(\mathbf{M}|\mathbf{D'}) \propto P(\mathbf{M})P(\mathbf{D'}|\mathbf{M}) \ . \tag{12}$$

From eq. (12), we know that the posterior probability density function of the model parameters is proportional to the product of the prior distribution of model parameters and the noise likelihood function. The main idea of Bayesian inversion is to determine the distribution of elastic parameters of subsurface media by estimating the maximum value of the posterior probability density function of the model parameters. Assuming that the regular noise such as multiple waves and converted waves in the pre-stack gathers has been removed, leaving only random noise $\mathbf{n}$ ($\mathbf{n} = \mathbf{D'}\text{-}\mathbf{GM}$), we can assume that the noise likelihood function obeys a Gaussian distribution:

$$P(\mathbf{D'}|\mathbf{M}) = ((2\pi)^{MN}|\mathbf{C_n}|)^{-\frac{1}{2}} \exp\left[-\frac{1}{2}(\mathbf{D'}\text{-}\mathbf{GM})^T \mathbf{C_n^{-1}}(\mathbf{D'}\text{-}\mathbf{GM})\right] \ , \tag{13}$$

where the matrix $\mathbf{C_n} = \sigma_n^2 \mathbf{I}$ represents the covariance matrix of the noise, σ_n^2 denotes the variance of the noise, and $\mathbf{I}$ is an $MN \times MN$ dimensional identity matrix.

The prior information reflects the statistical characteristics of the model parameters. The prior distributions of the model parameters can be assumed to have different statistical distributions (Gaussian probability distribution, Cauchy probability distribution, Huber probability distribution, etc.) and thus different inversion results can be obtained. Commonly, the prior distributions of model parameters can be divided into univariate and multivariate statistical distributions. However, when using a univariate statistical distribution as a prior constraint on model parameters, it is a necessary condition that the model parameters are independent of one another within the same sample. The multivariate group of statistical distributions includes

the multivariate Gaussian and the Trivariate Cauchy probability distributions. The multivariate Gaussian probability distribution provides a correlated AVO solution by introducing a covariance matrix of the three-term reflection coefficients. However, the Gaussian distribution can only generate constant weighting coefficients. In other words, it generates equal weighting coefficients for each reflection coefficient, so that the larger reflection coefficients cannot be emphasized and sparse solutions cannot be produced. In contrast, the Cauchy distribution can generate non-uniform weighting coefficients for each reflection coefficient during the inversion process, which can highlight large reflection coefficients and produce sparse solutions. Therefore, utilizing the Cauchy distribution as a prior constraint in the regularization term can generate sparse solutions, which can improve the resolution of the inverted results. The Trivariate Cauchy probability distribution is a special case of the multivariate t-distribution, which has three variables and one degree of freedom. The Trivariate Cauchy probability distribution of prior constraint can not only generate correlated AVO solutions, but can also provide sparse solutions. It is given by the following expression:

$$p(\mathbf{M}) = \prod_{i=1}^{N} \frac{2|\mathbf{\psi}|^{-1/2}}{\pi^2(1+\mathbf{M^T\Phi_i M})^2} \qquad \mathbf{\Phi_i} = \mathbf{D_i^T \psi^{-1} D_i} \tag{14}$$

where $\mathbf{\psi}$ is a correlation matrix that can be estimated using the expectation maximization algorithm of Alemie and Sacchi (2011), and $\mathbf{D_i}$ is a $3N \times 3N$ matrix, denoted as

$$\left[\mathbf{D_i}\right]_{xy} = \begin{cases} 1 & if\ x=1\ and\ y=i \\ 1 & if\ x=2\ and\ y=i+N \\ 1 & if\ x=3\ and\ y=i+2N \\ 0 & otherwise \end{cases} \quad . \tag{15}$$

Substituting the likelihood distribution in eq. (13) and the prior distribution in eq. (14) into eq. (12), we obtain a formula such as the one shown below:

$$p(\mathbf{M} \mid \mathbf{D'}) \propto \exp\left[-\frac{1}{2}(\mathbf{D'-GM})^T \mathbf{C_n^{-1}}(\mathbf{D'-GM})\right] \bullet \prod_{i=1}^{N} \frac{2|\mathbf{\psi}|^{-1/2}}{\pi^2(1+\mathbf{M^T\Phi_i M})^2} \tag{16}$$

By taking the logarithm of both sides of eq. (16), and carrying out some algebraic operations, the problem of estimating the maximum value of the posterior probability density function is transformed into minimizing the following equation:

$$F(\mathbf{M}) = \frac{1}{2}(\mathbf{D'} - \mathbf{GM})^T (\mathbf{D'} - \mathbf{GM}) + \mu \sum_{i=1}^{N} \ln(1 + \mathbf{M}^T \mathbf{\Phi}_i \mathbf{M}) \quad . \tag{17}$$

The first term on the right side of eq. (17) mainly controls the accuracy of inversion results; the second term on the right side of eq. (17) mainly controls the sparsity of inversion results; and $\mu = 2\sigma_n^2$ controls the weight of the prior distribution constraint of inversion. When μ is larger, the sparsity of the inversion results is higher. If the value of μ is too small, the accuracy of the inversion results will be degraded (Rabben and Ursin, 2000).

However, due to the noise, a single sparse-spike constraint is not sufficient to ensure the stability of the inversion results. By introducing a low-frequency constraint, the robustness of the inversion results can be improved. Conventionally, in many studies, a smoothing constraint is introduced for the low-frequency constraint. This smoothing constraint term $\mathbf{S}$ can be rewritten as

$$\begin{aligned}
\mathbf{S} &= \lambda_E (\mathbf{P_E M} - \mathbf{L_E})^T (\mathbf{P_E M} - \mathbf{L_E}) \\
&+ \lambda_\sigma (\mathbf{P_\sigma M} - \mathbf{L_\sigma})^T (\mathbf{P_\sigma M} - \mathbf{L_\sigma}) + \lambda_d (\mathbf{P_d M} - \mathbf{L_d})^T (\mathbf{P_d M} - \mathbf{L_d})
\end{aligned} \tag{18}$$

where λ_E, λ_σ, and λ_d are the weighting coefficients of the smoothing constraint for the Young's modulus, Poisson's ratio, and density reflectivity, respectively. $\mathbf{P_E}$, $\mathbf{P_\sigma}$, and $\mathbf{P_d}$ compose the integral matrices; taking $\mathbf{P_E}$ as an example, it can be expressed as

$$\mathbf{P_E} = \begin{bmatrix}
1 & 0 & \cdots & 0 & 0 & \cdots & 0 \\
1 & 1 & \cdots & 0 & 0 & \cdots & 0 \\
\vdots & \vdots & \cdots & \vdots & \vdots & \cdots & \vdots \\
1 & 1 & \cdots & 1 & 0 & \cdots & 0
\end{bmatrix}_{N \times 3N} , \tag{19}$$

and $\mathbf{L_E}$, $\mathbf{L_\sigma}$, and $\mathbf{L_d}$ are low-frequency components of the natural logarithm of the initial elastic parameters, which can be obtained from well-log data. Taking $\mathbf{L_E}$ as an example, it can be expressed as

$$\mathbf{L_E} = \begin{bmatrix} \ln\dfrac{E_2}{E_1} & \ln\dfrac{E_3}{E_1} & \cdots & \ln\dfrac{E_{N+1}}{E_1} \end{bmatrix}_{1 \times N}^T , \tag{20}$$

where E is the Young's modulus. Eq. (18) shows the minimum L2-norm of the differences between the natural logarithm of the inversion results and low-frequency components of the natural logarithm of the initial models. The inversion results approach the low-frequency components of the initial models to ensure that the inversion results have the correct low-frequency. However, this method may result in a reduction of the resolution of the inversion results. Therefore, we introduce a low-pass filter matrix $\mathbf{H}_i$ ($i = E$, σ, and d) to construct low-frequency constraints, and the specific expressions of low-pass filter matrices are given in Appendix C. Hence, the modified low-frequency constraint can be written as

$$\mathbf{S}' = \lambda_E (\mathbf{H_E P_E M} - \mathbf{L_E})^T (\mathbf{H_E P_E M} - \mathbf{L_E})$$
$$+ \lambda_\sigma (\mathbf{H_\sigma P_\sigma M} - \mathbf{L_\sigma})^T (\mathbf{H_\sigma P_\sigma M} - \mathbf{L_\sigma}) + \lambda_d (\mathbf{H_d P_d M} - \mathbf{L_d})^T (\mathbf{H_d P_d M} - \mathbf{L_d}) \tag{21}$$

Eq. (21) shows the minimum L2-norm of the differences between the low-frequency components of the natural logarithm of the inversion results and the low-frequency components of the natural logarithm of the initial models. The low-frequency components of the inversion results approach the low-frequency components of the initial models. Therefore, the modified low-frequency constraint does not affect the medium-frequency and high-frequency components of the inversion results. The modified low-frequency constraint can not only obtain reliable low-frequency components, but also does not reduce the resolution or accuracy of the inversion results. Then, the final objective function can be obtained as

$$F'(\mathbf{M}) = \frac{1}{2} (\mathbf{D'} - \mathbf{GM})^T (\mathbf{D'} - \mathbf{GM}) + \mu \sum_{i=1}^{N} \ln(1 + \mathbf{M^T \Phi_i M}) + \mathbf{S'} \tag{22}$$

Because eq. (22) is nonlinear, we use an iterative reweighted least-squares algorithm to solve the nonlinear expression. After obtaining the inversion results of the three-term reflectivity ($\mathbf{R_E}$, $\mathbf{R_\sigma}$, and $\mathbf{R_d}$), the values of three-term elastic parameters ($\mathbf{E}$, σ, and ρ) can be obtained by using the integral method, and it can be written as

$$\mathbf{E} = \mathbf{E_1} \exp\left[\int_{i=1}^{N} R_E(i)\right], \quad \sigma = \sigma_1 \exp\left[\int_{i=1}^{N} R_\sigma(i)\right], \quad \rho = \rho_1 \exp\left[\int_{i=1}^{N} R_d(i)\right]. \tag{23}$$

APPLICATIONS

Synthetic data test

The proposed method is applied to synthetic data derived from real model data (Fig. 2) for testing the superiority and the noise suppression of this inversion method. Based on the exact Zoeppritz equations, we use the elastic parameters given in Fig. 2 to calculate the P-wave reflection coefficients at different incident angles (from 10° to 50° with 10° intervals).

The synthetic seismogram shown in Fig. 3(a) is generated by a convolution of the calculated P-wave reflection coefficients with a Ricker wavelet whose dominant frequency is 35 Hz. To test the noise suppression of the proposed inversion method, we add random Gaussian noise to the synthetic data, with different signal-to-noise ratios (S/N): S/Ns of 10, 5, and 2 as represented in Figs. 3(b)–(d), respectively.

Fig. 4 shows that different low-frequency constraints can produce different inversion results. Figs. 4(a) and (b) represent the inversion results of modified low-frequency constraints and conventional low-frequency constraints, respectively, which apply the same prior Trivariate Cauchy constraint to the model parameters. The forward operators are based on approximate equations with an S/N of 5. Fig. 4(c) shows the error of the inversion results based on different low-frequency constraints. The accuracy of inversion results using the modified low-frequency constraints is higher than that of the conventional low-frequency constraints. In practice, the selection of the weighting coefficients of the conventional low-frequency constraint is usually based on the experience of the data processors who try to achieve the best inversion results by iteratively modifying the weighting coefficients. The conventional low-frequency constraint is very sensitive to the weighting coefficients, which can be subjective. However, the modified low-frequency constraint is relatively insensitive to the weighting coefficients and can improve the resolution and accuracy of the inversion results. Thus, it is preferable to use the modified low-frequency constraint in this context.

Figs. 5(a) − (h) illustrate the real (red line), initial (green line), and inverted (blue dotted line) Young's modulus, Poisson's ratio, and density curves. The inverted curves are the inversion results of the novel method proposed in this paper and the conventional method, with different S/Ns. The conventional method mentioned above is based on the approximate equations (Zong et al., 2013). We convert real logging data from logging scale to seismic scale using a Backus average (Backus and Gilbert, 1968, 1970) to obtain the real data. The initial model parameters are generated by smoothing the real model data. Fig. 5(a) displays the inversion results of the novel method based on the new exact equations and Fig. 5(b) presents the inversion results of the conventional method based on the approximate

equations. From Figs. 5(a) and (b), we find that the inversion results obtained by the conventional method are generally similar to the real data, but the results obtained by the new method are more accurate than those of conventional method, especially for Poisson's ratio and density. To test the stability of the new method, we add different degrees of noise to the pre-stack angle gathers. From Figs. 5(c) to 5(h), we can observe that the introduced noise has a great impact on the inversion results. As the noise increases, the error in the inverted elastic parameters also increases. However, for a given noise level, the inversion results of the new method proposed in this paper are more consistent with the actual data than the inverted results obtained using the conventional method.
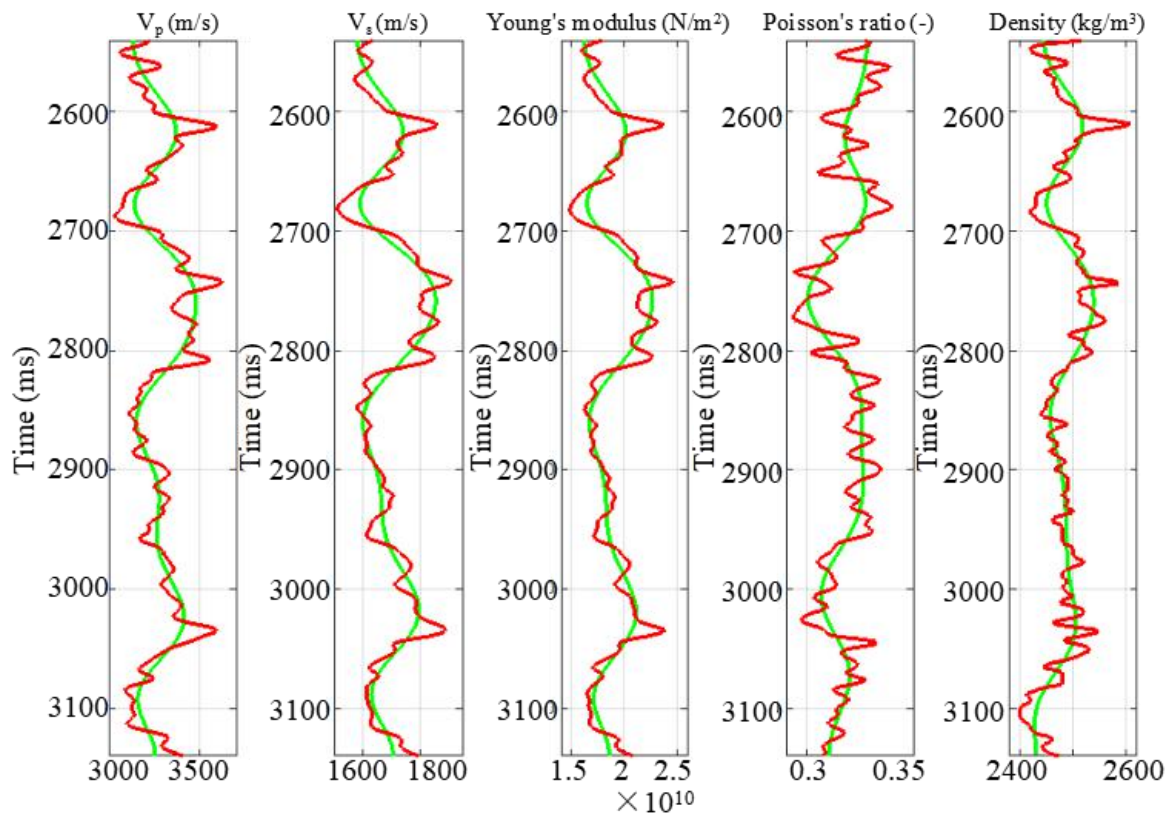
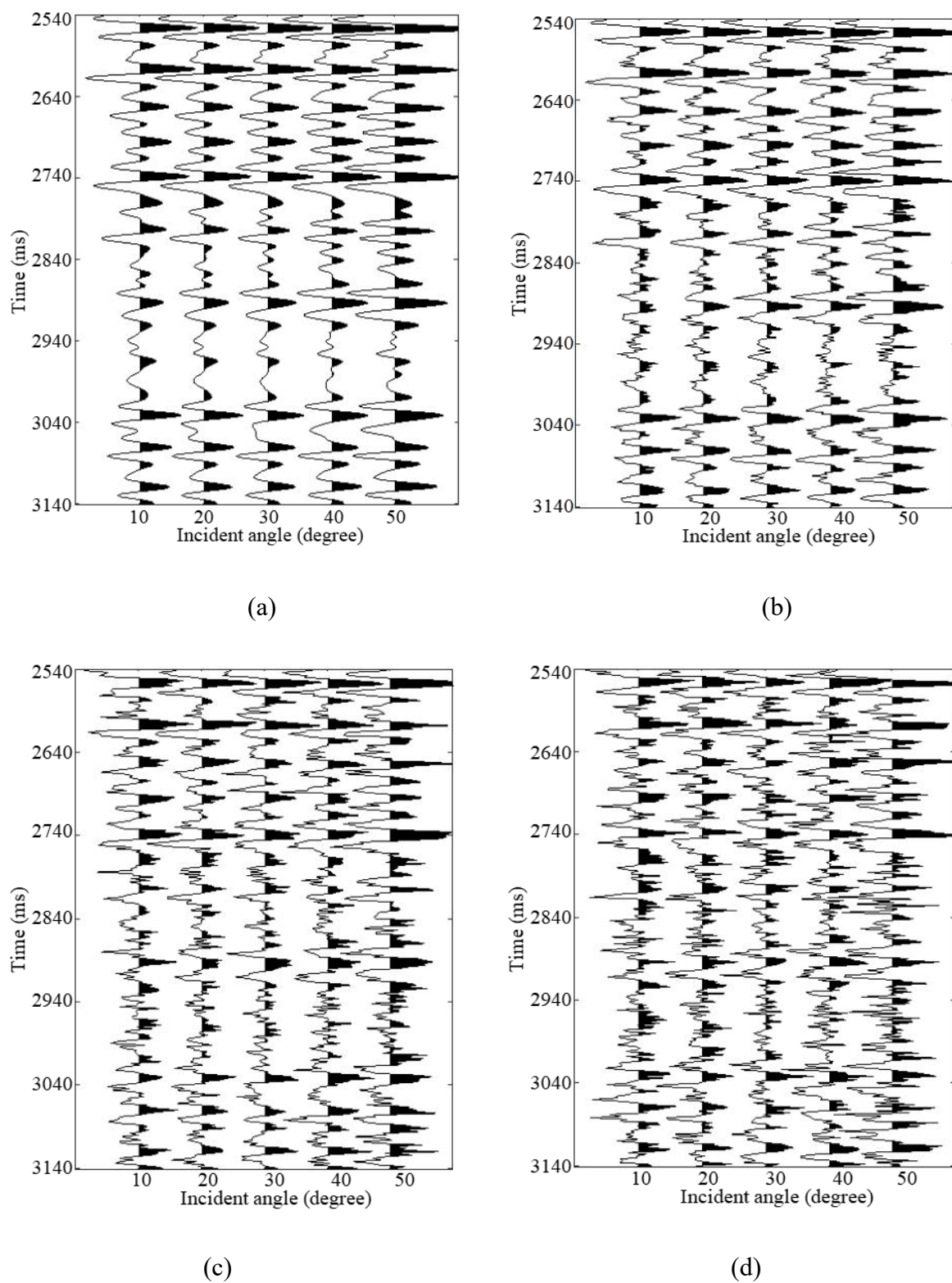Fig. 2. Real model data (red line) and initial model data (green line).

Fig. 3. Synthetic angle gathers with different S/Ns of known real data. (a) noise-free, (b) S/N = 10, (c) S/N = 5, (d) S/N = 2.
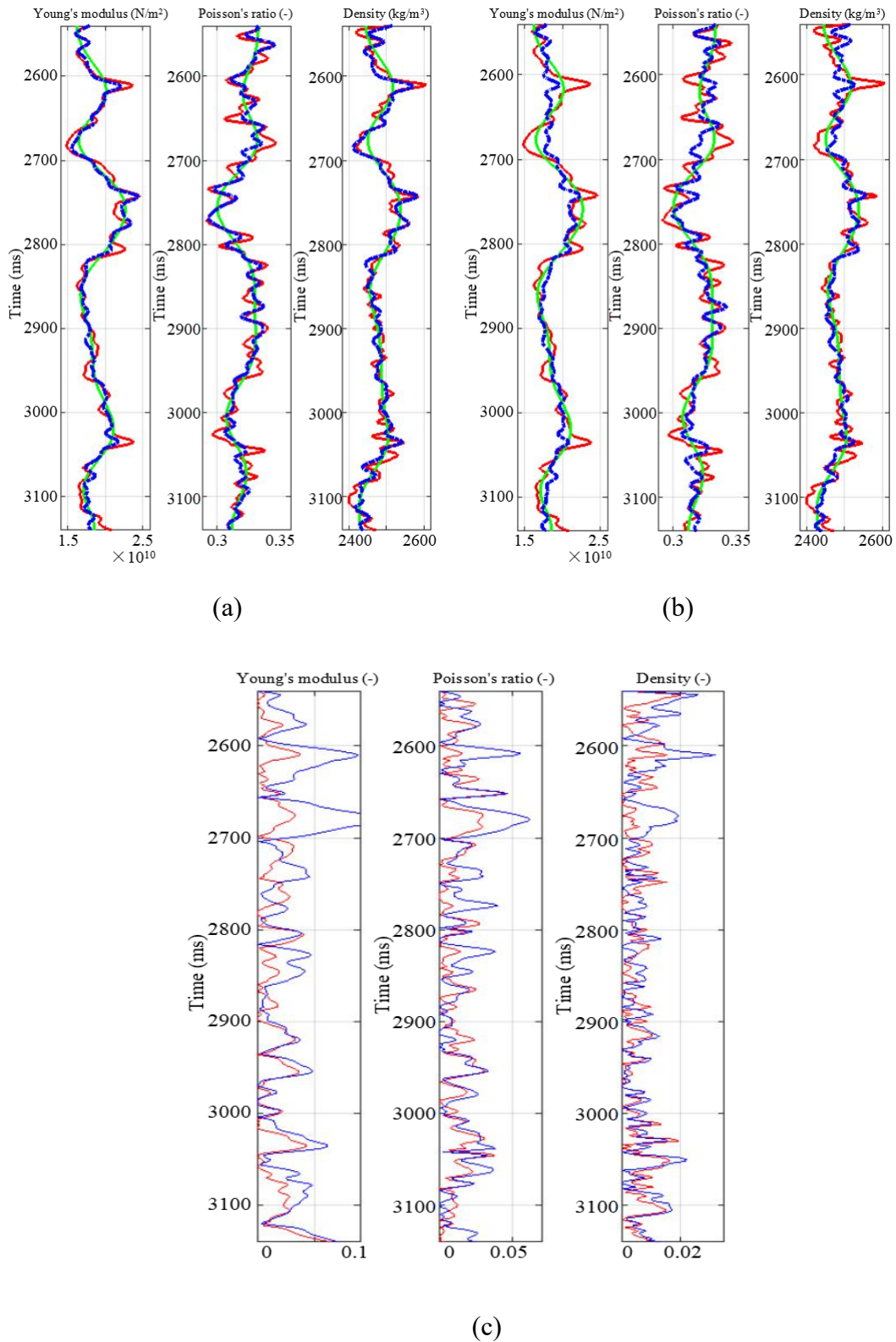
Fig. 4. Comparison of inversion results of different low-frequency constraints based on the approximate equations with an S/N of 5. (a) Inversion results with modified low-frequency constraints; (b) inversion results based on the conventional low-frequency constraints; (c) error traces for the inverted data: the red lines are the error traces of the inverted results based on the modified low-frequency constraints, and the blue lines are the error traces of the inversion results based on the conventional low-frequency constraints.
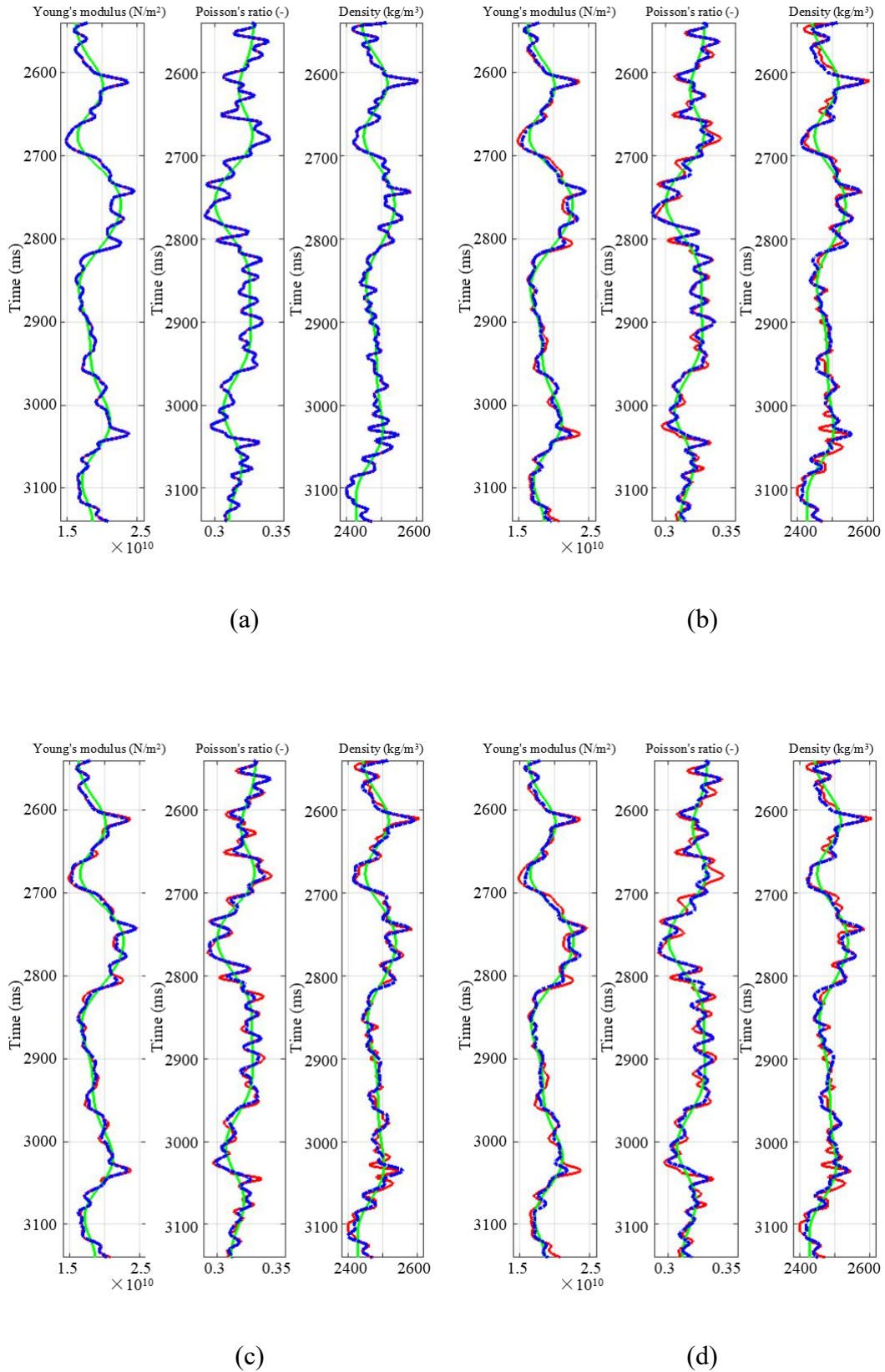
Fig. 5. Comparison of inversion results between the novel method and the conventional method with different S/Ns. (a) Inversion results based on the novel method with no noise; (b) inversion results based on the conventional method with no noise; (c) inversion results based on the novel method with an S/N of 10; (d) inversion results based on the conventional method with an S/N of 10:1.
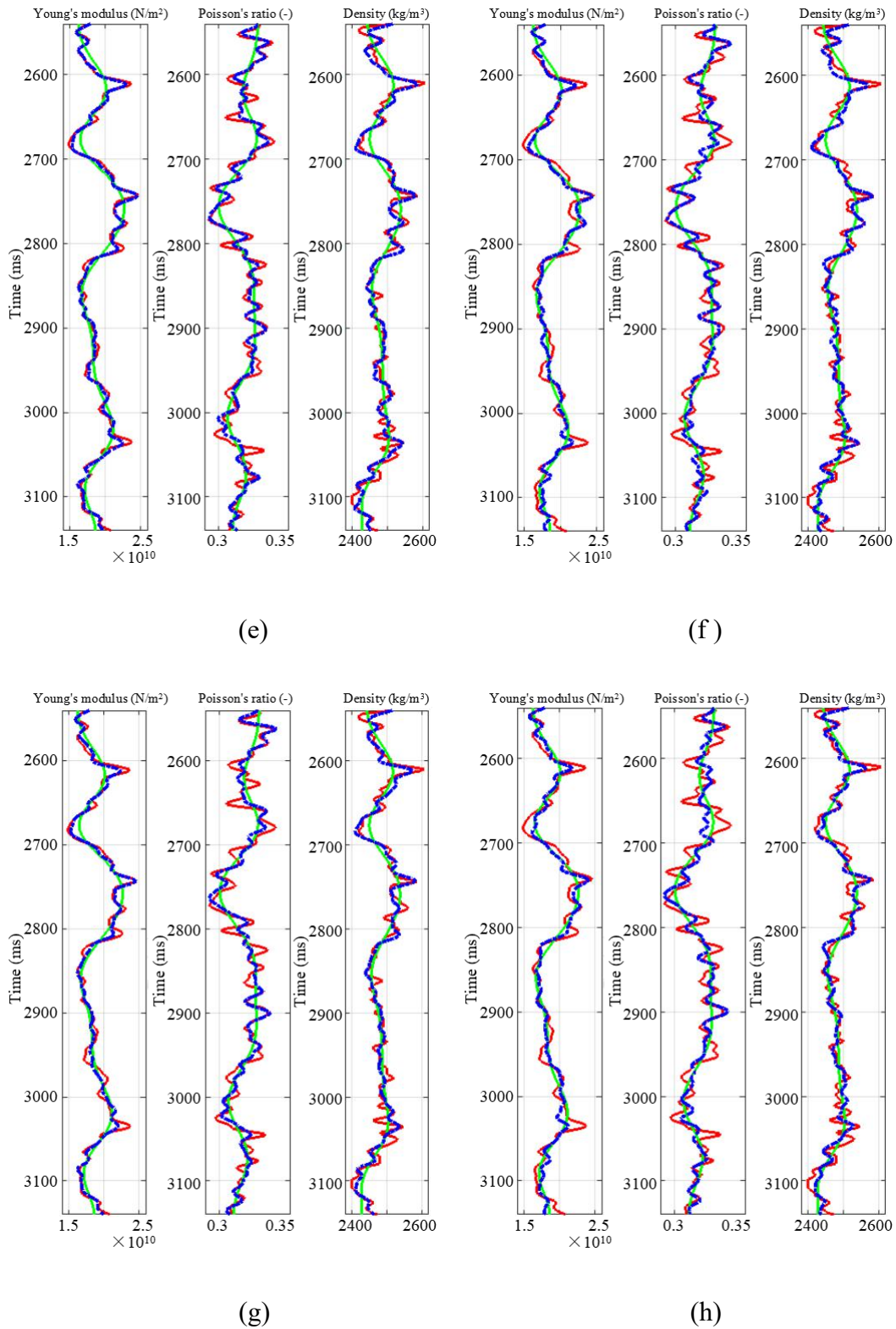
(e)

(f)

(g)

(h)

Fig. 5. Comparison of inversion results between the novel method and the conventional method with different S/Ns. (e) inversion results based on the novel method with an S/N of 5; (f) inversion results based on the conventional method with an S/N of 5; (g) inversion results based on the novel method with an S/N of 2; (h) inversion results based on the conventional method with an S/N of 2:1. In all plots, the red lines represent the real model parameters, the blue dotted lines are the inversion results, and the green lines indicate the initial model parameters.

Field data test

Next, the new inversion method mentioned above is applied to field data. To ensure that the final pre-stack information is as close as possible to the real subsurface information, the seismic data were processed by a series of amplitude-preserving procedures. Fig. 6 displays the seismic stack section, which is produced from the effective angle gathers (range of 4°–46°). The black line in Fig. 6 represents the trajectory of the known well. Based on the petrophysical analysis of the field data, we know that high-quality reservoirs are indicated by high Young's modulus, low Poisson's ratio, and low density in the target area. Using the logging data and geologic horizons, we can define initial models.
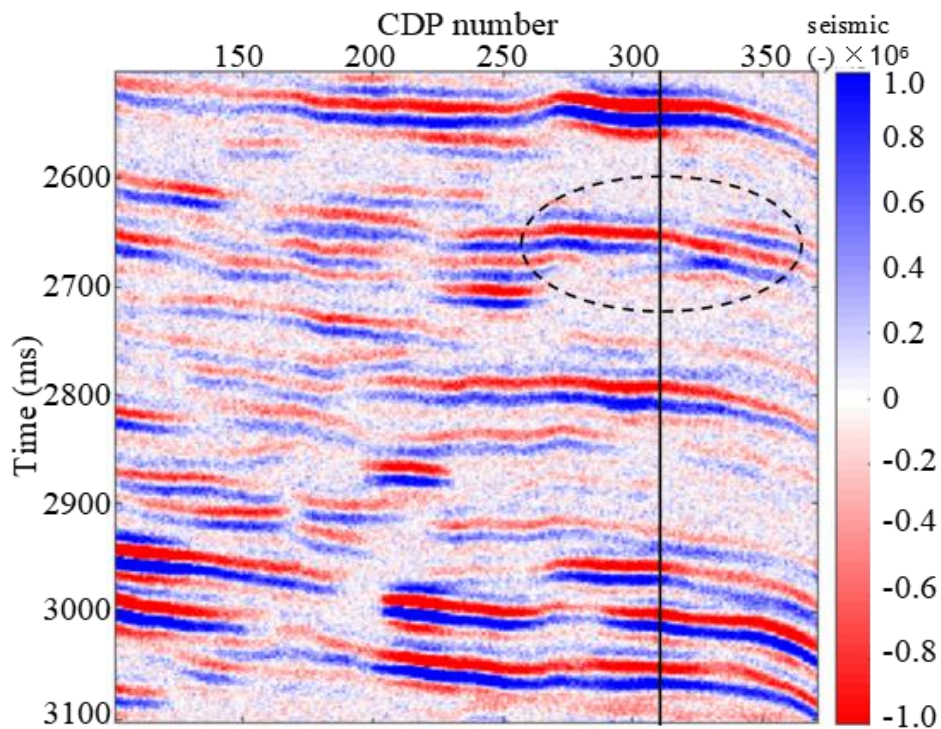

Fig. 6. Stacked seismic section from the field data used in the comparison. The black dotted ellipse represents the target reservoir.

Then, we used the conventional method and the proposed new method separately to invert the elastic parameters of the field data. The inverted Young's modulus, Poisson's ratio, and density sections based on the conventional method and proposed new methods are shown in Figs. 7 and 8, respectively. It is clear that the inversion results of the new method are better than those of the conventional method; the resolution of the results is also improved. To further compare the inverted parameters of the two methods, we extracted pseudo curves from the inverted results. The comparison of the

real logging curves and the pseudo curves is shown in Fig. 8. In Fig. 9, red lines indicate real logging curves, which are processed by a Backus average, the green lines present the pseudo curves of inverted results based on the conventional method, and the blue lines represent pseudo curves of inverted results based on the proposed method. In contrast, the inversion results obtained by the proposed method are closer to the true values than those obtained by the conventional method. Table 2 shows the correlation coefficients between the logging curves and pseudo curves of the conventional and proposed inversions. The inversion results of the new method are better-correlated with the real data. Therefore, it can be concluded that the method we propose is more stable and more consistent with the logged wireline data than the conventional method.
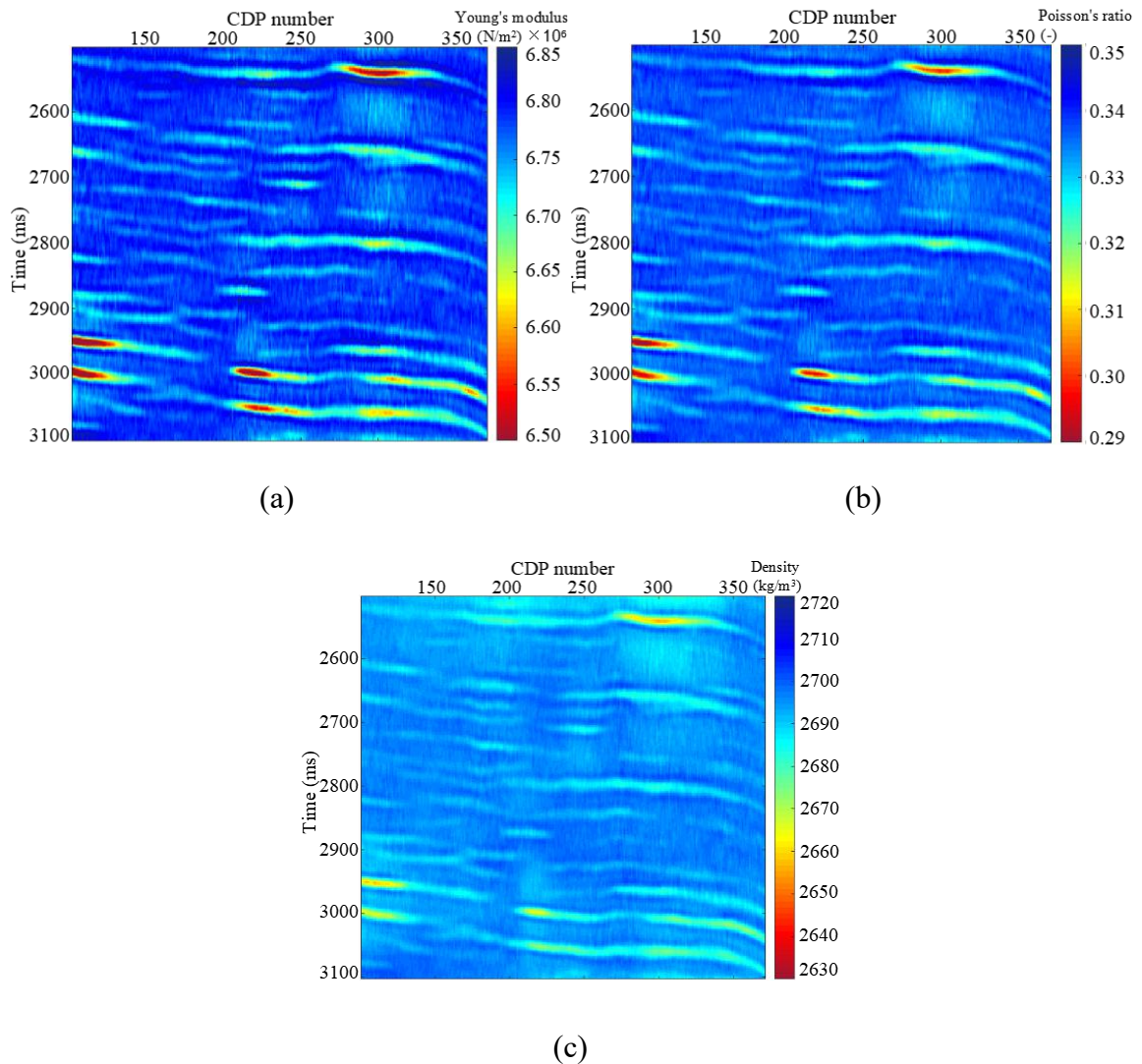

(a)

(b)

(c)

Fig. 7. Inverted seismic sections based on the conventional method. (a) profile of the inverted Young's modulus; (b) profile of the inverted Poisson's ratio; (c) profile of the inverted density.
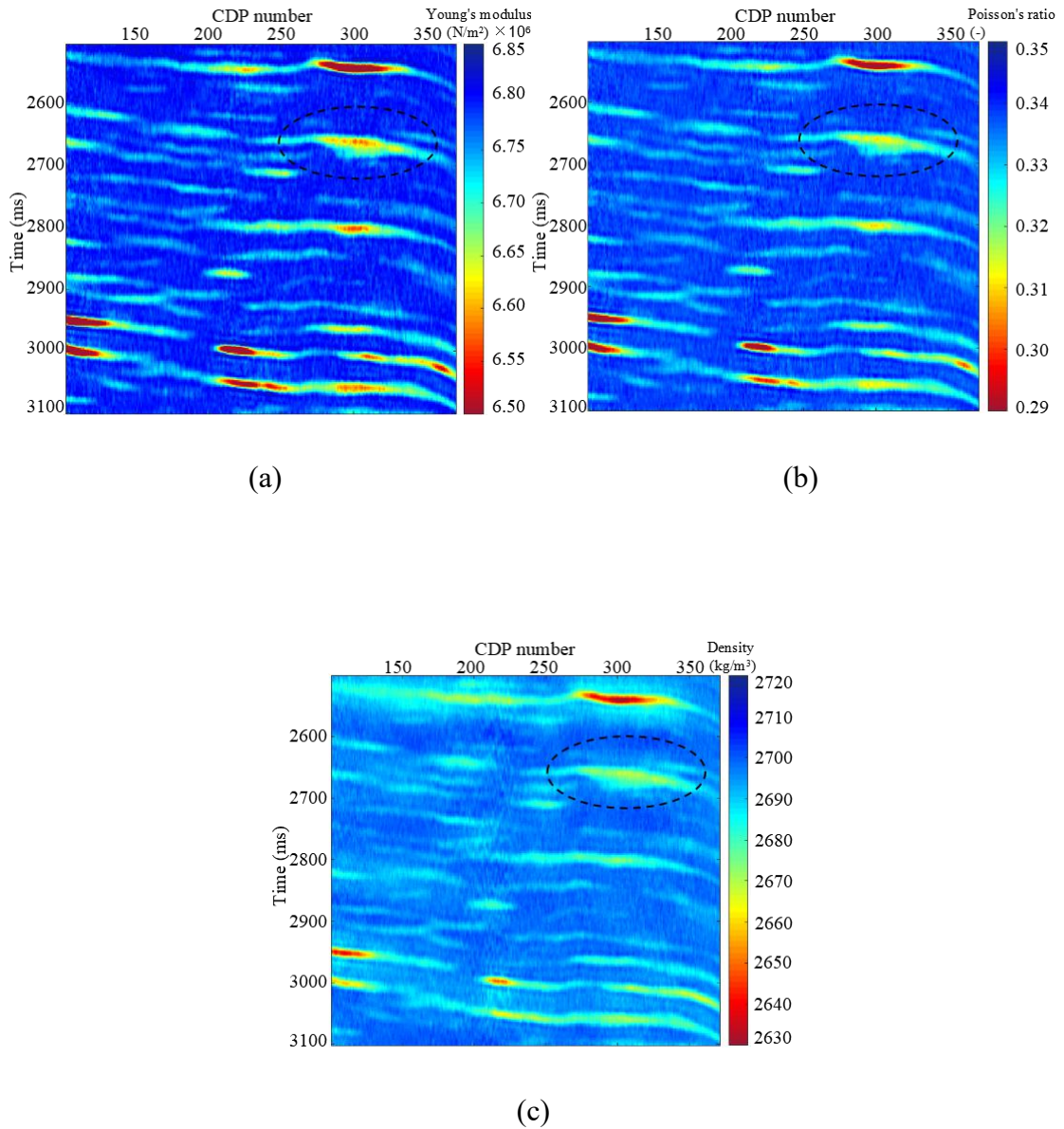
(a)

(b)

(c)

Fig. 8. Inverted seismic sections based on the novel method. (a) Profile of the inverted Young's modulus; (b) profile of the inverted Poisson's ratio; (c) profile of the inverted density.

Table 2. Correlation coefficients between the real logging curves and the pseudo curves of the inversion results.

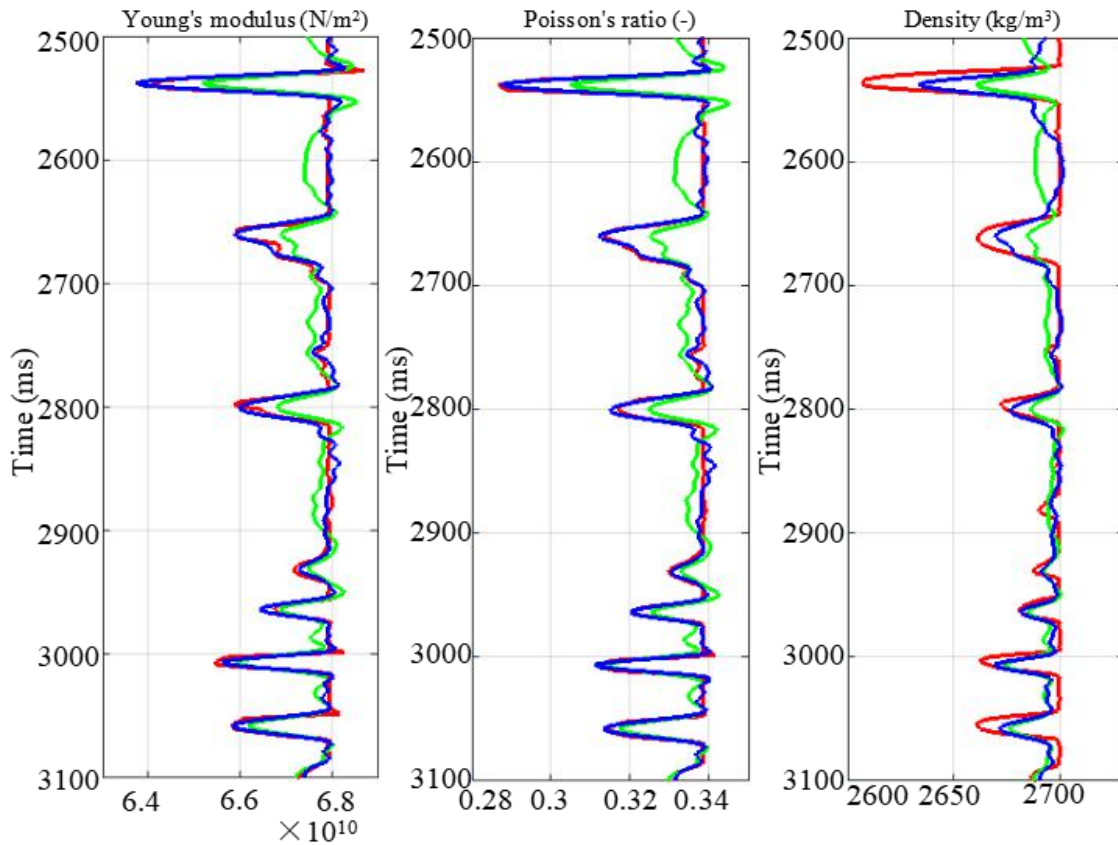| Method	Young's modulus	Poisson's ratio	Density
Proposed method	0.9653	0.9619	0.8565
Conventional method	0.9081	0.9012	0.7343

Fig. 9. Comparison of well-log curves in the time domain and the inverted results at the well location. The red lines indicate the real well-log data, the blue lines indicate the inversion results based on the method proposed in this paper, and the green lines indicate the inversion results based on the conventional method.

CONCLUSIONS

This study derived a set of novel exact Zoeppritz equations in terms of reflectivities defined as functions of Young's modulus, Poisson's ratio, and density in order to allow direct inversion for these parameters. Direct inversion can reduce the cumulative deviation more than conventional indirect inversion. The exact Zoeppritz equations were used to construct the forward operators to avoid the calculation error inherent in approximate equations, especially in the case of large angles of incidence.

The ill-conditioned inversion problem that results from the excessively large conditional number of the Jacobian matrix can be reduced effectively by incorporating Bayesian theory and introducing the prior distribution of the model parameters as a constraint in the inversion. This paper utilizes the Trivariate Cauchy probability distribution as a prior distribution to improve both the stability and the vertical resolution of the inversion. Furthermore, this study introduced a low-pass filter matrix to construct a low-frequency constraint term to obtain stable low-frequency information. The modified

low-frequency constraint does not reduce the vertical resolution or the accuracy of the inversion results, unlike the conventional low-frequency constraint.

Optimization of the objective function is achieved by utilizing the idea of the GLI and an iterative reweighted least-squares algorithm. With the help of these techniques, the accuracy and robustness of the inversion can be improved. Tests on both synthetic and field data illustrate that the proposed inversion method based on the new exact equations and the double constraints can obtain more stable and accurate values for Young's modulus, Poisson's ratio, and density than the conventional method.

ACKNOWLEDGEMENT

REFERENCES

Aki, K., Richards, P., 1980. Quantitative Seismology. W.H. Freeman & Co., New York.

Alemie, W. and Sacchi, M.D., 2011. High-resolution three-term AVO inversion by means of a trivariate Cauchy probability distribution. Geophysics, 76: R43-R55.

Altindag, R., 2002. The evaluation of rock brittleness concept on rotary blast hole drills. J. Sth. Afr. Inst. Min. Metall., 102: 61-66.

Avseth, P., Mukerji, T. and Mavko, G., 2005. Quantitative Seismic Interpretation. Cambridge University Press, Cambridge. doi.org/10.1017/CBO9780511600074

Backus, G.E. and Gilbert, F., 1968. The resolving power of gross earth data. Geophys. J. Roy. Astron. Soc., 16: 169-205.

Backus, G.E. and Gilbert, F., 1970. Uniqueness in the inversion of inaccurate gross earth data. Phil. Trans. Roy. Soc. Lond. A., 266: 123-192.

Bai, J., Xu, Z. and Xiao, Y.F., 2014. Nonlinear hybrid optimization algorithm for seismic impedance inversion. Chin. Petr. Soc. / SEG Internat. Geophys. Conf.: 541-544.

Behura, J., Kabir, N., Crider, R., Jilek, P. and Lake, E., 2010. Density extraction from P-wave AVO inversion. The Leading Edge, 29: 772–777.

Berkhout, A.J., 1997. Pushing the limits of seismic imaging, Part 1: Integration of pre-stack migration, velocity estimation, and AVO analysis. Geophysics, 62: 954-969.

Buland, A. and Omre, H., 2003. Bayesian linearised AVO inversion. Geophysics, 68: 185-198.

Castagna, J.P. and Backus, M.M., 1993. Offset-dependent Reflectivity: Theory and Practice of AVO Analysis. Vol. 8, Investigations in Geophysics. SEG, Tulsa, OK.

Castagna, J.P. and Swan, H.W., 1997. Principles of AVO crossplotting. The Leading Edge, 16: 337-342.

Cerney, B. and Bartel, D.C., 2007. Uncertainties in low-frequency acoustic impedance models. The Leading Edge, 26: 74-87.

Cooke, D.A. and Schneider, W.A., 1983. Generalised linear inversion of reflection seismic data. Geophysics, 48: 668-676.

Downton, J. E., 2005. Seismic parameter estimation from AVO inversion. Ph.D. thesis, University of Calgary.

Gidlow, M. and Smith, G.C., 2003. The fluid factor angle. Extended Abstr., 65th EAGE Conf., Stavanger: 2-5.

Guo, Z., Chapman, M. and Li, X., 2012. A shale rock physics model and its application in the prediction of brittleness index, mineralogy, and porosity of the Barnett Shale. Expanded Abstr., 82nd Ann. Internat. SEG Mtg., Las Vegas: 1-5.

Haitham, H. and Adam, P., 2015. Multitrace impedance inversion with lateral constraints. Geophysics, 80: M101-M111.

Huang, H.D., Wang, Y.C., Guo, F., Zhang, S., Ji, Y.Z. and Liu, C.H., 2015. Zoeppritz equation-based pre-stack inversion and its application in fluid identification. Appl. Geophys., 12: 199-211.

Lu, J., Yang, Z., Wang, Y. and Shi, Y., 2015. Joint PP and PS AVA seismic inversion using exact Zoeppritz equations. Geophysics, 80: R239-R250. doi:10.1190/GEO2014-0490.1.

Karimi, O., Omre, H. and Mohammadzadeh, M., 2010. Bayesian closed-skew Gaussian inversion of seismic AVO data for elastic material properties. Geophysics, 75: 1-11.

Khare, V., 2007. Density Inversion Using Joint PP/PS Data: Sensitivity to the Angle Range. Expanded Abstr., 77th Ann. Internat. SEG Mtg., San Antonio: 965-969.

Knott, C.G., 1899. Reflexion and refraction of elastic waves with seismological applications. Phil. Mag., 48: 64-97.

Kurt, H., 2007. Joint inversion of AVA data for elastic parameters by bootstrapping. Comput. Geosci., 33: 367-382. doi.org/10.1016/j.cageo.2006.08.012.

Larsen, J.A., 1999. AVO Inversion by simultaneous P-P and P-S inversion. M.Sc. Thesis, University of Calgary.

Li, G.L., Chen, G. and Zhong, J.Y., 2013. Analysis of geophone properties effects for land seismic data. Appl. Geophys., 6: 91-101.

Li, L.M., Luo, X.X. and Wang, M.C., 2010. 3D PP-PS joint inversion method and application in an isotropic medium. Chin. J. Geophys. (in Chinese), 45: 60-65.

Liu, F.P., Meng, X.J., Wang, Y.M., Shen, G.Q. and Xiao, J.Q., 2012. Multi-angle inversion of formation densities based on the accurate solutions of Zoeppritz's partial derivative equations．Chin. J. Geophys. (in Chinese), 55: 252-259. doi: 10.6038/ j. Issn.0001-5733. 2012.01.024

Liu, Z.S. and Sun, Z.D., 2015. New brittleness indexes and their application in shale/clay gas reservoir prediction. Petr. Explor. Dev., 42: 117-124.

Mavko, G., 2010. Rock physics of shale. Stanford Rock Phys. Lab., Stanford, CA.

Ostrander, W.J., 1984. Plane-wave reflection coefficients for gas sands at non-normal angles of incidence. Geophysics, 49: 1637-1648.

Priezzhev, I.I. Shmaryan, L.E. and Bejarano, G., 2008. Non-linear multitrace seismic inversion using neural network and genetic algorithm-genetic inversion. Extended Abstr., 70th EAGE Conf., Rome: 137-145.

Quakenbush, M., Shang, B. and Tuttle, C., 2006. Poisson impedance. The Leading Edge, 25: 128-138.

Rabben, T.E. and Ursin, B., 2000. Non-linear least-squares inversion with data-driven Bayesian regularization. Geophys. J. Internat., 142: 43-72.

Rickman, R., Mullen, M., Petre, E., Greiser, B. and Kundert, B., 2008. A practical use of shale petrophysics for stimulation design optimization: All shale plays are not clones of the Barnett Shale. SPE 115258. SPE Ann. Techn. Conf., Denver, CO.

Ritesh, K.S. and Chopra, S., 2013. Using a new seismic attribute for determination of lithology and brittleness. CSEG Rec. 38.

Sena, A., Castillo, G., Chesser, K., Voisey, S., Estrada, J., Carcuz, J. and Schneider, R.V., 2011. Seismic reservoir characterization in resource shale plays: "Sweet spot" discrimination and optimization of horizontal well placement Expanded Abstr., 81st Ann. Internat. SEG Mtg., San Antonio: 1744-1748.

Shi, Y., Yao, F., Sun, H. and Qi, L., 2010. Density inversion and porosity estimation using seismic data. Chin. J. Geophys., 53: 197-204.

Shuey, R.T., 1985. A simplification of the Zoeppritz equations. Geophysics, 50: 609-618.

Sun, Z.D., Jia, C.Z. and Li, X.F., 2011. Unconventional Oil and Gas Exploration and Development (in Chinese). Beijing: Publicat. Petroleum Indust.: 865-970.

200

Tarantola, A., 1986. A strategy for nonlinear elastic inversion of seismic reflection data. Geophysics, 51: 1893-1903. doi.org/10.1190/1.1442046.

Tao, Z.F., Zhao, Y.L. and Ma, L., 2011. Low frequency seismic and low frequency vibrator. EGP, 21(2): 71-76.

Tian, J., Wu, G.C. and Zong, Z.Y., 2013. Robust three-term AVO inversion and uncertainty analysis. OGP (in Chinese). 48: 443-449.

Veeken, P.C., Priezzhev, I.I., Shmaryan, L.E., Shteyn Y.I., Barkov A.Y. and Ampilov Y.P., 2009. Nonlinear multitrace genetic inversion applied on seismic data across the Shtokman field offshore northern Russia. Geophysics, 74: 49-59.

Yang, Z., Hou, L.H., Tao, S.Z., Cui, J.W., Wu, S.T., Lin, S.H. and Pan, S.Q., 2015. Formation conditions and "sweet spot" evaluation of tight oil and shale oil. Petr. Explor. Dev., 42: 555-565.

Yang, P. and Yin, X., 2008. Pre-stack seismic inversion method based on support vector machine. J. China Univ. Petrol., 32: 37-41.

Yuan, S., Wang, S. and Tian, N., 2009. Swarm intelligence optimization and its application in geophysical data inversion. Appl. Geophys., 6: 166-174.

Zhang, F.Q., Jin, Z.J., Sheng, X.J. and Kong, L.W., 2016. Bayesian pre-stack three-term inversion with soft low-frequency constraint. OGP (in Chinese), 51: 965-975.

Zhang, H.B., Shang, Z.P. and Yang, C.C., 2007. A non-linear regularised constrained impedance inversion. Geophys. Prosp., 55: 819-833.

Zhang, J.H., Zhang, B.B., Zhang, Z.J., Liang, H.X. and Ge, D.M., 2015. Low-frequency data analysis and expansion. Appl. Geophys., 12: 212-220.

Zhou, L., Li, J.Y. and Chen, X.H., 2016. Nonlinear three-term AVO inversion based on exact Zoeppritz equations. Chin. J. Geophys. (in Chinese), 59: 2663-2673. doi:10.6038/cjg 20160729.

Zhou, L., Li, J., Chen, X., Liu, X. and Chen, L., 2017. Pre-stack AVA inversion of exact Zoeppritz equations based on modified trivariate Cauchy distribution. J. Appl. Geophys., 138: 80-90.

Zoeppritz, K.B., 1919. On reflection and transmission of seismic waves by surfaces of discontinuity. Nachrichten der Königlichen Gesellschaft der Wissenschaften zu Göttingen, Mathematisch-physikalische Klasse. (in German): 66-84.

Zong, Z.Y., Yin, X.Y. and Wu, G.C., 2012. Reflection coefficient equation and pre-stack seismic inversion with Young's modulus and Poisson ratio. Chin. J. Geophys. (in Chinese), 55: 3786-3794. doi: 10.6038/j.issn.0001-5733.2012.11.025.

Zong, Z., Yin, X. and Wu, G., 2013. Elastic impedance parameterization and inversion with Young's modulus and Poisson's ratio. Geophysics, 78: N35-N42. doi: 10.1190/geo2012-0529.1.

APPENDIX A

The complex nonlinear problem can be simplified by Taylor's first-order expansion of the P-wave reflection coefficient, R_{pp}, in terms of the initial P-wave reflection coefficient R_{pp0}; hence, we obtain the following function:

$$R_{pp} = R_{pp0} + \frac{\partial R_{pp0}}{\partial R_E} \Delta R_E + \frac{\partial R_{pp0}}{\partial R_\sigma} \Delta R_\sigma + \frac{\partial R_{pp0}}{\partial R_d} \Delta R_d \quad , \qquad \text{(A-1)}$$

where R_{pp} is the actual observed reflection coefficient of P-wave, R_{pp0} is the

P-wave reflection coefficient calculated from the initial model parameters of Poisson's ratio reflectivity $R_{\sigma 0}$, Young's modulus reflectivity R_{E0} , and density reflectivity R_{d0} . $\dfrac{\partial R_{pp0}}{\partial R_E}$, $\dfrac{\partial R_{pp0}}{\partial R_\sigma}$, and $\dfrac{\partial R_{pp0}}{\partial R_d}$ represent the first-order partial derivatives of R_{pp0} with respect to R_E , R_σ , and R_d , respectively; the specific expressions are given in Appendix B. On the basis of the convolutional model, the wavelet ω is introduced on both sides of the eq. (A-1), yielding

$$d - d_0 = g \varDelta m \quad , \tag{A-2}$$

where

$$d = R_{pp} * \omega , \quad d_0 = R_{pp0} * \omega \quad ,$$

and

$$g = [\frac{\partial R_{pp0}}{\partial R_E} * \omega, \frac{\partial R_{pp0}}{\partial R_\sigma} * \omega, \frac{\partial R_{pp0}}{\partial R_d} * \omega] , \quad \varDelta m = [\varDelta R_E, \varDelta R_\sigma, \varDelta R_d]^T .$$

Additionally, d represents the observed seismic data, d_0 is the synthetic seismic data obtained from initial models, $\varDelta m$ denotes the perturbations of the model parameters. Clearly, $\varDelta m$ can be calculated by eq. (11); however, the prior distribution of $\varDelta m$ is unknown. If $\varDelta m$ is used as the inversion parameter, the constraints of inversion cannot be constructed. The prior distribution of $m = [R_E, R_\sigma, R_d]^t$ can be defined, thus we select m as the inversion model parameter. By adding gm_0 simultaneously to both sides of eq. (A-2), the inversion parameter is converted from $\varDelta m$ to m:

$$d - d_0 + gm_0 = gm \quad . \tag{A-3}$$

If we consider M angles and N samples per trace, eq. (A-3) will be written as

$$\mathbf{D} \text{-} \mathbf{D_0} + \mathbf{GM_0} = \mathbf{GM} \quad , \tag{A-4}$$

where

$$\mathbf{D} = [\mathbf{D}(\boldsymbol{\theta}_1), \mathbf{D}(\boldsymbol{\theta}_2)...\mathbf{D}(\boldsymbol{\theta}_M)]^T_{MN\times 1}, \quad \mathbf{D}(\boldsymbol{\theta}_i) = [d(\theta_i, t_1), d(\theta_i, t_2)...d(\theta_i, t_N)]^T_{N\times 1}$$

$$\mathbf{D_0} = [\mathbf{D_0}(\boldsymbol{\theta}_1), \mathbf{D_0}(\boldsymbol{\theta}_2)...\mathbf{D_0}(\boldsymbol{\theta}_M)]^T_{MN\times 1}, \quad \mathbf{D_0}(\boldsymbol{\theta}_i) = \mathbf{W}(\boldsymbol{\theta}_i)\mathbf{R_{pp0}}(\boldsymbol{\theta}_i)$$

$$\mathbf{R_{pp0}}(\boldsymbol{\theta}_i) = [R_{pp0}(\theta_i, t_1), R_{pp0}(\theta_i, t_2),...R_{pp0}(\theta_i, t_N)]^T_{N\times 1}$$

$$\mathbf{G} = \begin{bmatrix} \mathbf{W}(\boldsymbol{\theta}_1)\mathbf{G_E}(\boldsymbol{\theta}_1) & \mathbf{W}(\boldsymbol{\theta}_1)\mathbf{G_\sigma}(\boldsymbol{\theta}_1) & \mathbf{W}(\boldsymbol{\theta}_1)\mathbf{G_d}(\boldsymbol{\theta}_1) \\ \mathbf{W}(\boldsymbol{\theta}_2)\mathbf{G_E}(\boldsymbol{\theta}_2) & \mathbf{W}(\boldsymbol{\theta}_2)\mathbf{G_\sigma}(\boldsymbol{\theta}_2) & \mathbf{W}(\boldsymbol{\theta}_2)\mathbf{G_d}(\boldsymbol{\theta}_2) \\ \vdots & \vdots & \vdots \\ \mathbf{W}(\boldsymbol{\theta}_M)\mathbf{G_E}(\boldsymbol{\theta}_M) & \mathbf{W}(\boldsymbol{\theta}_M)\mathbf{G_\sigma}(\boldsymbol{\theta}_M) & \mathbf{W}(\boldsymbol{\theta}_M)\mathbf{G_d}(\boldsymbol{\theta}_M) \end{bmatrix}_{MN\times 3N}$$

$$\mathbf{W} = \begin{bmatrix} \omega(\theta_i, t_1) & 0 & \cdots & 0 \\ \omega(\theta_i, t_2) & \omega(\theta_i, t_1) & \cdots & 0 \\ \vdots & \vdots & \ddots & \vdots \\ \omega(\theta_i, t_N) & \omega(\theta_i, t_{N-1}) & \cdots & \omega(\theta_i, t_1) \end{bmatrix}_{N\times N}$$

$$\mathbf{M_0} = \begin{bmatrix} \mathbf{R_{E0}} \\ \mathbf{R_{\sigma 0}} \\ \mathbf{R_{d0}} \end{bmatrix}_{3N\times 1}, \quad \mathbf{M} = \begin{bmatrix} \mathbf{R_E} \\ \mathbf{R_\sigma} \\ \mathbf{R_d} \end{bmatrix}_{3N\times 1}$$

Additionally, θ_i is the M-th incident angle, and t_N is the N-th sample of the seismic trace. $\mathbf{W}(\boldsymbol{\theta}_i)$ represents the extracted seismic wavelet matrix with the incident angle θ_i. $\mathbf{G_E}(\boldsymbol{\theta}_i)$, $\mathbf{G_\sigma}(\boldsymbol{\theta}_i)$, and $\mathbf{G_d}(\boldsymbol{\theta}_i)$ represent the diagonal matrices of the first-order partial derivatives of R_{pp0} with respect to R_E, R_σ, and R_d, respectively. We take $\mathbf{G_E}(\boldsymbol{\theta}_i)$ as an example, where

$$\mathbf{G_E}(\boldsymbol{\theta}_i) = \begin{bmatrix} \left.\frac{\partial R_{pp0}}{\partial R_E}\right|^{\theta_i}_{t_1} & 0 & \cdots & 0 \\ 0 & \left.\frac{\partial R_{pp0}}{\partial R_E}\right|^{\theta_i}_{t_2} & \cdots & 0 \\ \vdots & \vdots & \ddots & \vdots \\ 0 & 0 & \cdots & \left.\frac{\partial R_{pp0}}{\partial R_E}\right|^{\theta_i}_{t_N} \end{bmatrix}_{N\times N}$$

$\mathbf{M}_0$ represents the matrix of the initial model parameters; taking $\mathbf{R}_{E0}$ as an example, it can be expressed as

$$\mathbf{R_{E0}}(\mathbf{\theta}_i) = [R_{E0}(\theta_i, t_1), R_{E0}(\theta_i, t_2), ... R_{E0}(\theta_i, t_N)]_{1 \times N}^T$$

$\mathbf{M}$ represents the matrix of the model parameters; taking $\mathbf{R}_E$ as an example, it can be expressed as

$$\mathbf{R_E}(\mathbf{\theta}_i) = [R_E(\theta_i, t_1), R_E(\theta_i, t_2), ... R_E(\theta_i, t_N)]_{1 \times N}^T$$

To simplify eq. (A-4), it can be written as

$$\mathbf{D'} = \mathbf{D} - \mathbf{D}_0 + \mathbf{GM}_0 = \mathbf{GM} \quad . \tag{A-5}$$

APPENDIX B

The new exact equations in terms of the Young's modulus , Poisson's ratio and density reflectivities can be expressed as

$$\begin{bmatrix} \sin a & \cos b & -\sin a' & \cos b' \\ \cos a & -\sin b & \cos a' & \sin b' \\ \sin 2a & \gamma \cos 2b & \dfrac{(2+A)^2(2+C)(2-B)\sin 2a'}{(2-A)^2(2-C)(2+B)} & -\dfrac{(2+A)(2+C)\gamma\cos 2b'}{(2-A)(2-C)} \\ \cos 2b & -\dfrac{\sin 2b}{\gamma} & -\dfrac{(2+B)(2+C)\cos 2b'}{(2-B)(2-C)} & -\dfrac{(2+A)(2+C)\sin 2b'}{(2-A)(2-C)\gamma} \end{bmatrix} \begin{bmatrix} R_{pp} \\ R_{ps} \\ T_{pp} \\ T_{ps} \end{bmatrix} = \begin{bmatrix} -\sin a \\ \cos a \\ \sin 2a \\ -\cos 2b \end{bmatrix}$$

$$\tag{B-1}$$

where

$$A = \frac{1}{2}\left(R_E + \frac{(k-2)^2(3k-2)}{k(3k-4)}R_\sigma - R_d\right),$$

$$B = \frac{1}{2}\left(R_E + \frac{2-k}{3k-4}R_\sigma - R_d\right),$$

and $\qquad C = R_d .$

For convenience, eq. (B-1) can be written as follows:

$$\mathbf{ZR} = \mathbf{C} \tag{B-2}$$

where $\mathbf{Z}$ is the coefficient matrix of eq. (B-1), $\mathbf{R}$ represents the reflection coefficient and the transmission coefficient terms of eq. (B-1), and $\mathbf{C}$ denotes the constant term on the right side of eq. (B-1). Then, by taking the first derivative of eq. (B-2) with respect to R_E, R_σ, R_d, we can obtain the following expressions:

$$\frac{\partial \mathbf{R}}{\partial R_E} = -\mathbf{Z}^{-1} \frac{\partial \mathbf{Z}}{\partial R_E} \mathbf{R} , \quad \frac{\partial \mathbf{R}}{\partial R_\sigma} = -\mathbf{Z}^{-1} \frac{\partial \mathbf{Z}}{\partial R_\sigma} \mathbf{R} , \quad \frac{\partial \mathbf{R}}{\partial R_d} = -\mathbf{Z}^{-1} \frac{\partial \mathbf{Z}}{\partial R_d} \mathbf{R} \qquad \text{(B-3)}$$

By solving eq. (B-3), the first-order partial derivatives of the P-wave reflection coefficients with respect to R_E, R_σ, and R_d can be obtained.

APPENDIX C

The specific expression of the low-pass filter matrix $\mathbf{H}$ of the low-frequency constraint can be written as

$$\mathbf{H} = \mathbf{K}^T \mathbf{F}^{-1} \mathbf{\Lambda} \mathbf{F} \mathbf{K} \qquad \text{(C-1)}$$

In eq. (C-1), the matrix $\mathbf{K}$ plays the role of extending the model parameters by 3 times. The mathematical expression of the $\mathbf{K}$ matrix is

$$\mathbf{K} = \begin{bmatrix} 0 & & 1 \\ & \mathinner{\mkern2mu\raise1pt\hbox{.}\mkern2mu\raise4pt\hbox{.}\mkern2mu\raise7pt\hbox{.}\mkern1mu} & \\ 1 & & 0 \\ & \ddots & \\ 0 & & 1 \\ & \mathinner{\mkern2mu\raise1pt\hbox{.}\mkern2mu\raise4pt\hbox{.}\mkern2mu\raise7pt\hbox{.}\mkern1mu} & \\ 1 & & 0 \end{bmatrix}_{(N-2) \times N} \qquad \text{(C-2)}$$

$\mathbf{F}$ and $\mathbf{F}^{-1}$ are the positive and inverse transform matrices of a discrete Fourier transformation (DFT), respectively, they can provide a Fourier transform and a Fourier inverse transform of the data. The $\mathbf{\Lambda}$ matrix in eq. (C-1) is a diagonal matrix composed of Hanning window functions.